Research Article Vol. 30, No. 3 / 31 Jan 2022 / Optics Express 4424
Optics EXPRESS

Wide-angle and broadband solar absorber made using highly efficient large-area fabrication strategy

WENJIE HOU, FAN YANG, ZEMING CHEN, JIANWEN DONG, AND SHAOJI JIANG*

State Key Laboratory of Optoelectronic Materials and Technologies, School of Physics, Sun Yat-sen University, Guangzhou 510275, China
*stsjsj@mail.sysu.edu.cn

Abstract: High performance and cost-effective solar absorbers are crucial for various optical applications, such as solar collection and thermophotovoltaic devices. This study designs and experimentally demonstrates a wide-angle and broadband solar absorber. The proposed absorber is composed of tapered polyimide substrate and Al-Cr-SiO_2-Cr-SiO_2 thin-film based on the optical interference of the multilayer thin film and excited magnetic resonance of light-trapping structures. The composite process of the colloidal lithography method and magnetron sputtering is employed for efficient fabrication in a large area. The average absorbance is more than 93% from 300 nm to 2500 nm and shows an angular tolerance of up to 60°. The high efficiency and large-area fabrication capability demonstrated by the proposed solar absorber presents future application potential in flexible solar collection devices.

1. Introduction

Solar energy has gained considerable attention since it is clean and abundant and also due to the environmental deterioration caused by fossil energy along with its limited availability. Broadband solar absorbers are crucial for capturing solar energy and are widely employed in optical applications, such as photocatalysis [1–3], photodetection [4–6], and solar collection devices [7–13]. An ideal solar broadband absorber is required to absorb the full spectrum of solar radiation under arbitrary polarization states and incident angles in order to efficiently harvest the solar energy, considering the unpolarized and diffusive characteristics of sunlight. Therefore, a wide-angle and broadband solar absorber presents considerable practical significance.

Various methods have been proposed in previous studies to broaden the absorption bandwidth, such as multiple electromagnetic resonances [9,14–20], slowlight waveguide modes [21–23], gap plasmon [24–26], and the use of broadband intrinsic loss metals [27–29]. Furthermore, high structural symmetry and the excitation of surface plasmon polaritons reduce the sensitivity to the polarization state and incident angle. A comparison of the state-of-art wide-angle and broadband absorbers is shown in Table 1. Some absorbers present the potential of large-area fabrication, but their absorption performance needs to be improved, such as the operating bandwidth and the angular tolerance. Additionally, part of the absorbers show excellent absorption performance, but they are unable to be efficiently fabricated in large-area due to the time-consuming and costly nanofabrication technologies. This indicates that designing wide-angle and broadband solar absorbers compatible with the currently used cost-effective industrial production technology remains a major challenge.

This study presents the design of a wide-angle and broadband solar absorber fabricated using a large-area fabrication strategy. The proposed absorber is composed of tapered polyimide (PI) substrate and Al-Cr-SiO_2-Cr-SiO_2 thin-film and is based on the optical interference of a multilayer thin film and the excited magnetic resonance of a light-trapping structure. The centimeter-scale

#451411 https://doi.org/10.1364/OE.451411
Journal © 2022 Received 16 Dec 2021; revised 12 Jan 2022; accepted 17 Jan 2022; published 26 Jan 2022

Optics EXPRESS

Table 1. A comparison of the state-of-art wide-angle and broadband absorbers

	Bandwidth	Average absorption	Angular tolerance	Experimental / simulation methods
Chen et al. [16]	400–700 nm	>94%	A_{ave} >70% (0°- 60°)	Nanoimprinting lithography and electroforming technology (Exp.)
Chen et al. [31]	350–1170 nm	>97%	A_{ave} > 95% (0°- 50°)	Magnetron sputtering (Exp.)
Jiang et al. [10]	380–1910nm	>98%	A_{ave} >88% (0°- 60°)	Spin-coating and magnetron sputtering (Exp.)
Zhang et al. [18]	500–1750nm	>90%	A_{ave} >90% (0°- 40°)	Magnetron sputtering, electron beam lithography and inductively coupled plasma (Exp.)
Liu et al. [19]	570–3539 nm	>97%	A_{ave} > 80% (0°- 50°)	Finite-difference time-domain (Sim.)
Liu et al. [20]	300–1100 nm	>97%	A_{ave} >95% (0°- 40°)	Finite-difference time-domain (Sim.)
This work	300–2500 nm	>93%	A_{ave} >88.5% (0°- 60°)	Colloidal lithography and magnetron sputtering (Exp.)

(2.5 cm × 2.5 cm) absorber is efficiently fabricated using the colloidal lithography method and magnetron sputtering composite process. It can absorb solar radiation between 300 nm and 2500 nm with high average absorbance of more than 93%. Furthermore, it remains unaffected by the incident angle and polarization state. The bending resistance of the sample is experimentally demonstrated, and its absorption performance exhibits minimal variation after the bending tests. Additionally, the proposed high performance solar absorber presents considerable potential for application in flexible solar collection devices.

2. Design and fabrication

Figure 1(a-b) presents the three-dimensional schematic and cross-sectional view of the proposed absorber, which is based on the multilayer thin-film absorbers and light-trapping absorbers, both of which present advantages and disadvantages. The multilayer thin-film absorbers can be easily and efficiently fabricated using a large-area fabrication strategy. However, they are sensitive to the incident angle and their absorption bandwidth is limited by the materials used for fabrication [30–32]. The light-trapping absorbers exhibit excellent absorption performance at the cost of a high aspect ratio gap, which presents considerable challenges in their fabrication [25,33]. Consequently, the multilayer thin film and the tapered flexible PI substrate are integrated to obtain the proposed absorber in this study in order to overcome the aforementioned drawbacks. The period (P), height (h_1), and bottom and top diameters (W_1, W_2) of the truncated cone are set as 500 nm, 500 nm, 450 nm, and 150 nm, respectively, and the thickness of each layer of the five-layer thin film from bottom to top (h_2, h_3, h_4, h_5, h_6) is set as 25 nm, 50 nm, 50 nm, 10 nm, and 50 nm, respectively.

The fabrication process employs the microspheres self-assembly technology, reactive ion etching (RIE-501, Jingshengweian Technology), and magnetron sputtering (MSP-300, Jingshengweian Technology), as shown in Fig. 1(c). Firstly, the PI substrate is ultrasonically cleaned in ethanol for 20 minutes to enhance its hydrophilicity. The 10%wt polystyrene (PS) microspheres (500 nm) aqueous solution and equal volume ethanol mixture is then added to deionized water mixed with 30uL 10%wt sodium dodecyl sulfate (SDS). The PS microspheres are self-assembled into a large-area and hexagonal close-packed monolayer on the water-air interface due to the surface tension and capillary force. This monolayer is transferred to the prepared PI substrate. Secondly, the SF_6 and O_2 RIE are performed successively after 24 hours of drying in the air. The

Optics EXPRESS

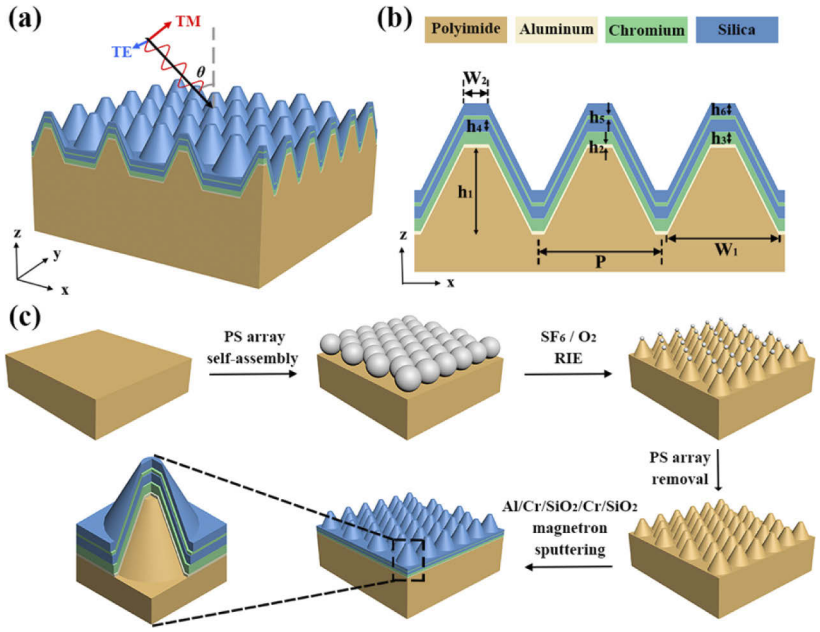

Fig. 1. (a) 3D schematic and (b) cross-sectional configuration of the proposed absorber. (c) Schematic of the steps involved in the fabrication.

SF_6 RIE is primarily used to fluorinate the PI substrate, while the O_2 RIE is used to reduce the size of the PS microspheres and etch the PI substrate. The RIE are performed under a pressure of 2 Pa, an SF_6 /O_2 gas flow rate of 15/50 SCCM and RF power of 60W; the time of both processes is set as 500 s. The remaining PS microspheres were removed by ultrasonic cleaning in ethanol for 400s. So far, the tapered PI substrate is successfully prepared. Lastly, the five-layer thin film is deposited on the tapered PI substrate through the magnetron sputtering process and Table 2 presents the detailed parameters of the process. Consequently, a large-area (2.5 cm × 2.5 cm) absorber is efficiently fabricated.

Table 2. Parameters of magnetron sputtering

Sputtering Sequence	Pressure (Pa)	Power (W)	Time (s)
Al	0.5	60	450
Cr	0.5	10	750
SiO_2	0.5	250	500
Cr	0.5	10	150
SiO_2	0.5	250	500

3. Simulation results and discussion

The proposed absorber shown in Fig. 1(a-b) is set up and systematically calculated by FDTD Solutions from LUMERICAL. In the simulation, the optical constants of Al and Cr are obtained from the Lorentz-Drude model using the experimental table data [34], the optical constant of SiO_2 is obtained from Ref. [35], and the permittivity of PI is obtained from Refs. [36,37]. The absorbance (A), is calculated by $A = 1 - R - T$, where R and T represent the reflectance and transmittance, respectively, based on the conservation of energy.

Optics EXPRESS

Figure 2(a) depicts the simulated reflectance, transmittance, and the calculated absorbance of the proposed absorber when TM-polarized light is normally incident. The simulated transmittance is close to zero since the thickness of the Al layer and the bottom Cr layer are much thicker than the penetration depth. The proposed absorber exhibits a high absorbance, greater than 90% in the range of 300 nm to 1970nm and the average absorbance is 93% in the range of 300 nm to 2500 nm, covering most of the solar spectrum. Figure 2(b) shows the absorbed and missed solar energy obtained through the absorbance of the proposed absorber and the spectral intensity of solar radiation in order to further clarify the response of the absorber to solar irradiation. Consequently, the absorbed solar energy curve almost entirely encompasses the solar spectral profile and the missed solar energy is close to zero, which indicates that the solar energy is almost absorbed. Furthermore, the absorbance of different polarization states is calculated at normal incidence as shown in Fig. 2(c). There is almost no difference between them due to the rotational symmetry of the designed structure. This result verifies the polarization-independence of the proposed absorber. The absorption spectrum is calculated for unpolarized light [$A_{unpolarized} = (A_{TM} + A_{TE})/2$] at different oblique incident angles, varying from 10° to 60° in 5° steps to determine the absorption performances related to incident angle. The range of absorbance exceeding 90% narrows slightly with the increase in the incident angle, as shown in Fig. 2(d). However, the average absorbance from 300 nm to 2500 nm still remains at 88.5% at an incident angle of 60°, which indicates that the proposed absorber is unaffected by the incident angle.

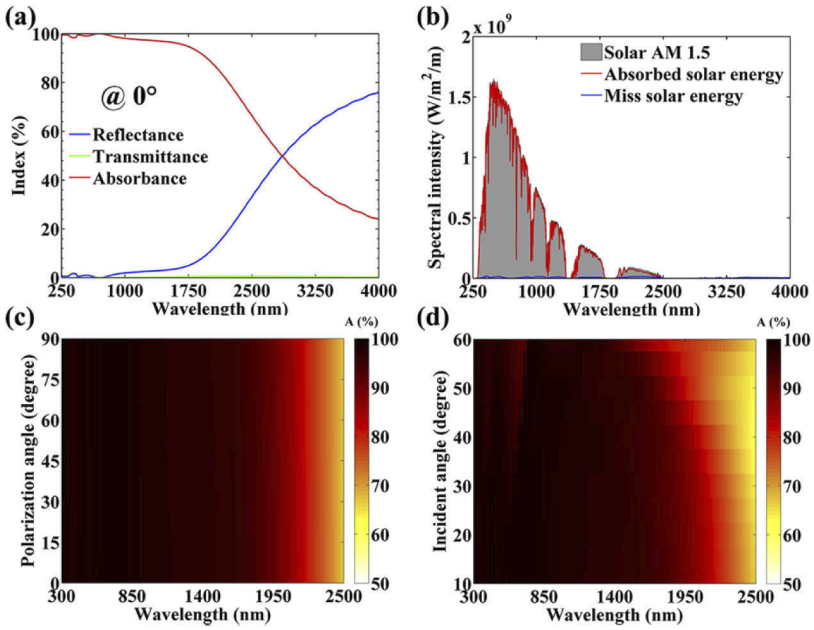

Fig. 2. (a) Simulated reflectance, transmittance, and the corresponding calculated absorbance of the proposed absorber at normal incidence for TM-polarized light. (b) Absorption efficiency of the proposed absorber under solar irradiation with the AM 1.5 source. (c) Calculated absorbance for different polarization angles from 0° to 90° at normal incidence. (d) Simulated absorption spectrum at different incident angles varying from 10° to 60° in 5° steps for unpolarized light.

The absorber is designed based on multilayer thin films and light-trapping structures. The simulated absorbance of the planar absorber is compared with the same thin film, the Cr light-trapping structure with same parameters, and the absorber, as shown in Fig. 3. The planar absorber has high absorbance only in the short wavelength, based on the optical interference of

Optics EXPRESS

the multilayer thin film and the Cr light-trapping structure can achieve near perfect absorption in the broadband by exciting the magnetic resonance. The proposed absorber presents the best absorption performance due to the joint effect of optical interference of the multilayer thin film and the excited magnetic resonance of the light-trapping structure.

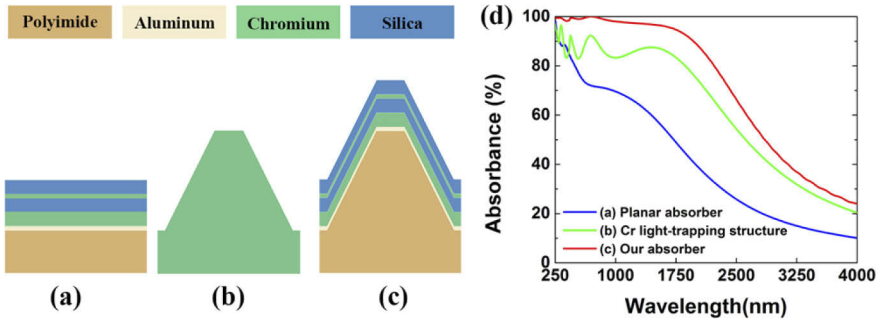

Fig. 3. Cross-sectional configuration of (a) planar absorber, (b) Cr light-trapping structure, and (c) the proposed absorber. (d) Comparison of the calculated absorbance of these absorbers.

The cross section of the magnetic field and the heat power density at the specific wavelengths of 500 nm, 1000 nm, and 1500 nm are further calculated and described in Fig. 4 to further illustrate the underlying mechanism of the proposed absorber. The heat power density, q, is calculated by $q = \frac{1}{2}\varepsilon_0\omega\varepsilon''|E|^2$, where ε_0, ω, ε'' and E represent the vacuum permittivity, angular frequency of the electromagnetic field, relative permittivity of the metal and local electric field, respectively.

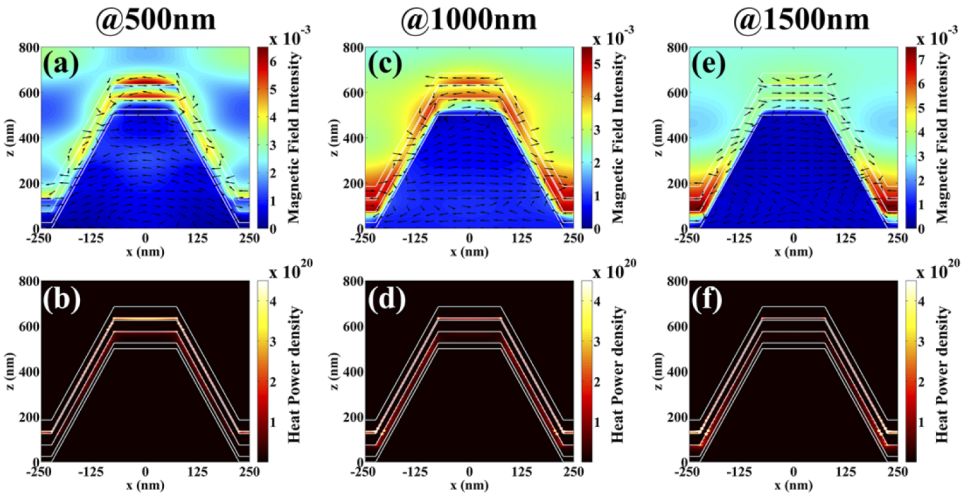

Fig. 4. Contour of the magnetic field intensity (a, c, e) and the heat power density (b, d, f) at normal incidence for TM-polarized light with different incident wavelength. The arrows shown in (a, c, e) represent the direction of electric displacement.

At the short wavelength (500 nm), the strong magnetic field is primarily confined to the interface between SiO_2 and Cr at the top of the proposed absorber due to the intrinsic loss property of Cr, as shown in Fig. 4(a). Furthermore, the F-P cavity composed of the top Cr layer, middle SiO_2 layer, and bottom Cr layer can trap energy, based on the optical interference theory. The top SiO_2 layer reduces the reflection to allow for more light to enter the F-P cavity based on

Optics EXPRESS

impedance matching and also protects the absorber from oxidation. Consequently, most of the energy is absorbed by the top layer of the proposed absorber, as shown in Fig. 4(b).

At the long wavelength (1500 nm), the enhanced magnetic field is localized at the bottom layer of the absorber as shown in Fig. 4(e), which can be attributed to the excitation of magnetic polaritons (MPs). An inductor-capacitor (LC) circuit can be used to analyze MPs and the resonance wavelength can be predicted by $\lambda_R = 2\pi c_0\sqrt{LC}$, where the inductive elements, L, and the capacitive elements, C, are related to the metal layer and the dielectric part [17]. The capacitance increases with the decrease in the gap between the structural units [9]. Therefore, the magnetic resonance generated by the electric displacement loop slowly moves to the bottom of absorber with the increase in the incident wavelength. Most of the energy is thus dissipated at the bottom of the proposed absorber, as shown in Fig. 4(f).

The localized magnetic field on the upper and lower sidewall of the absorber is observed at the same time at the medium wavelength (1000 nm), as shown in Fig. 4(c). Furthermore, the amplitude of magnetic field is smaller than that at the short and long wavelengths. The effect of the optical interference reduces while the localized magnetic field due to the MPs increases with the increase in the incident wavelength based on the absorption mechanism explained earlier. It can thus be inferred that the high absorption performance at the medium wavelength depends on the joint effect of both the optical interference and excited magnetic resonance, due to which most of the energy is absorbed evenly by the upper and lower sidewall as shown in Fig. 4(d).

4. Experimental results

The scanning electron microscope (SEM) images of the prepared samples are characterized by the electron beam lithography scanning electron microscope (EBL-SEM, Pioneer Two, Raith). An ultrathin Pt layer is deposited on the surface to improve the conductivity of the samples.

PS microspheres with a diameter of 500 nm formed a hexagonally close-packed monolayer on the 2.5 cm × 2.5 cm PI substrate, which act as a mask in the subsequent etching process, as shown in Fig. 5(a-b). Figure 5(c-d) depicts the prepared tapered PI substrate after the SF_6 / O_2 RIE and ultrasonic cleaning processes. The height and the top and bottom diameters of the truncated cones are approximately 475 nm, 180 nm and 440 nm, respectively. The parameters of the truncated cones can be adjusted by the etching parameters. A blank silicon wafer is placed next to the sample during magnetron sputtering to quantitatively measure the thickness of each layer of the five-layer thin film. The five-layer thin film is uniformly deposited on the sample, presenting a negligible change in the morphology of the sample, as shown in Fig. 5(e-f). The photograph of the prepared sample appears black, as shown in Fig. 5(g), indicating that it has good absorption performance in the visible regime. Figure 5(h) presents the cross-section of the five-layer planar structure. The thickness of each layer, from bottom to top, is approximately 25 nm, 45 nm, 45 nm, 13 nm, and 43 nm, respectively. It can be concluded that the parameters of the prepared sample correspond well to the design of the proposed absorber based on the SEM images presented above.

The transmittance is close to zero since the thickness of the Al layer and the bottom Cr layer are much greater than the penetration depth. Therefore, the measured absorbance is calculated as $A = 1 - R$. The absorption performance of the sample is tested by measuring the reflection spectrum using a UV-VIS-NIR spectrophotometer (Lambda950, Wavetest) equipped with the absolute specular reflectance accessory. The absorption performance of the oblique incidence is tested from 8° to 60°, as it is limited by the spectrophotometer. Figure 6(a) presents the comparison between the simulated and measured absorbance from 300 nm to 2500 nm at nearly normal incidence (8°) for unpolarized light. Figure 6(b) presents the measured absorbance at different oblique incident angles varying from 10° to 60° in steps of 5°. It can be concluded that the measured results correspond well with the simulated results in the range of 300 nm to 2000nm, based on Fig. 6(a) and the comparison between Figs. 2(d) and 6(b). However, the measured

Optics EXPRESS

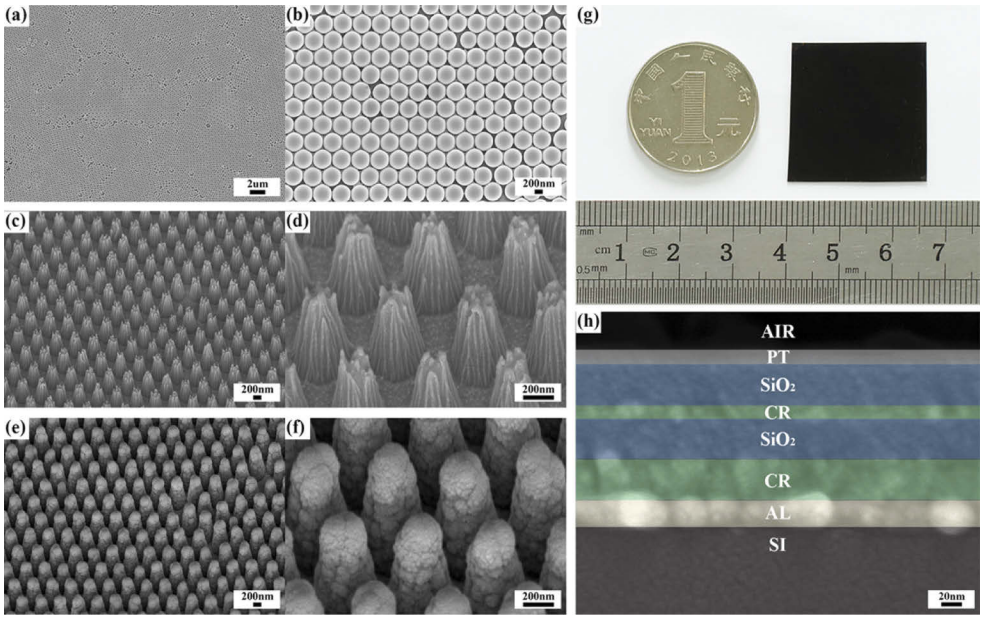

Fig. 5. (a-b) SEM images of monolayer hexagonal PS microsphere arrays at 0° with different scale. (c-d) SEM images of tapered PI substrate at 45° with different scale. (e-f) SEM images of the proposed absorber at 45° with different scale. (g) Photograph of prepared sample at 0°. (h) Cross-section SEM image of the planar five-layer thin film deposited together with the proposed absorber.

absorbance is higher than the simulated absorbance from 2000nm to 2500 nm. This is mainly due to the presence of some metal nanoparticles on the sample surface during magnetron sputtering, which excites the localized surface plasmon [11,14,15]. Additionally, Fig. 6(c) presents the photograph of the prepared sample taken at angles of 20°, 40°, and 60° under indoor illumination conditions. This sample always appears black at different viewing angles, indicating that it presents angular tolerance.

Flexible solar absorbers are generally applied on non-planar surfaces. Multiple bending typically results in the release of stress which can destroy the microstructure very easily. Therefore, the bending resistance of prepared sample is tested. The sample can bend both outward and inward indicating that it has mechanical flexibility, as shown in Fig. 7(a). The bending test is performed on a platform with adjustable clamping distance to determine its bending resistance. The prepared sample remains black even when it is almost folded in half, as depicted in the inset of Fig. 7(b). Furthermore, the morphology of the prepared sample is characterized by SEM technology after performing the bending tests 1000 times to observe the impact of the bending tests. A slight crack marked by the white rectangle, appears on the surface of prepared sample, as shown in Fig. 7(c). Additionally, the absorption spectrum of the prepared sample is compared before and after the 1000 iterations of bending tests, as shown in Fig. 7(b). There is almost no difference in the absorption spectrum at nearly normal incidence (8°) or oblique incidence (60°), indicating that cracks have a negligible effect on the absorption performance of the prepared sample.

Optics EXPRESS

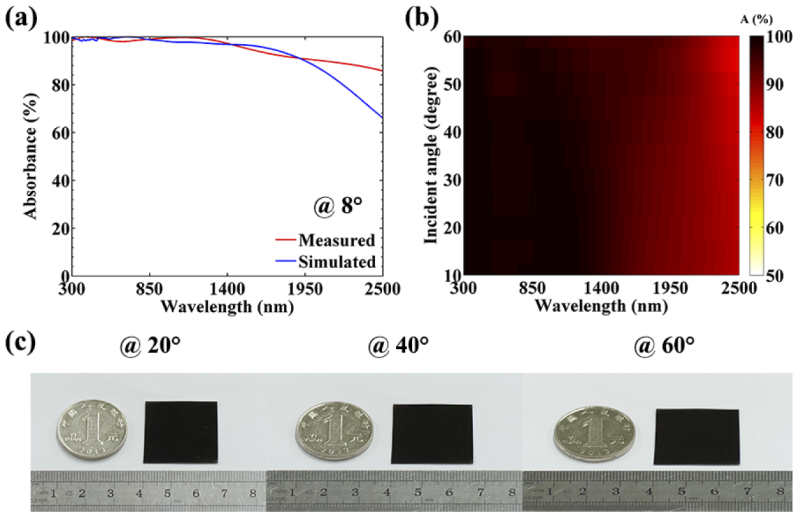

Fig. 6. (a) The comparison between calculated and measured absorbance at an incident angle of 8° for unpolarized light. (b) Measured absorption spectrum of prepared sample at different incident angles varying from 10° to 60° in 5° steps for unpolarized light. (c) Photograph of prepared sample taken with indoor ambient light at angles of 20°, 40°, 60°.

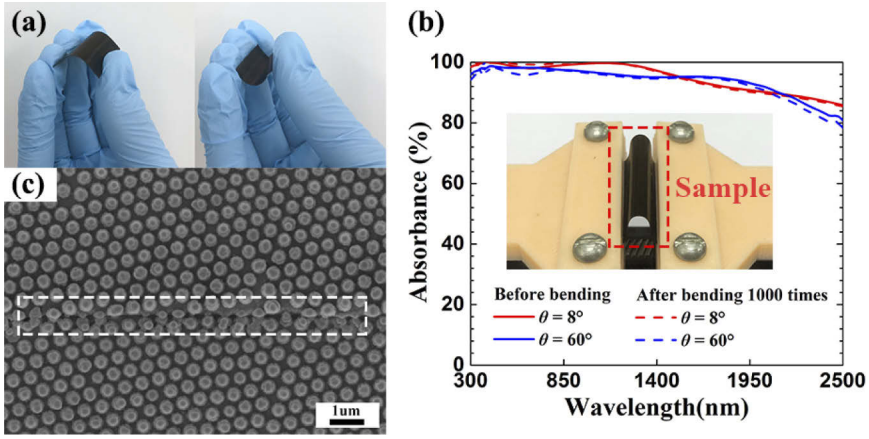

Fig. 7. (a) Photograph of prepared sample during bending outward and inward. (b) Measured absorption spectrum before and after 1000 times of bending tests at an incident angle of 8° and 60° for unpolarized light. The inset is the photography of the bending test. (c) SEM image of sample after 1000 times of bending test at 0°.

5. Conclusions

In summary, this study presents the design of a wide-angle and broadband solar absorber based on the optical interference of multilayer thin films and the excited magnetic resonance of light-trapping structures. A centimeter-scale (2.5 cm × 2.5 cm) absorber is efficiently fabricated through the composite process of the colloidal lithography method and magnetron sputtering. The proposed absorber absorbs solar radiation between 300 nm and 2500 nm with high average absorbance exceeding 93%, indicating that the solar energy is almost absorbed. Furthermore, the proposed absorber is unaffected by the polarization state and incident angle. The average absorption remains as high as 88.5% even when the incident angle is increased to 60°, which

Optics EXPRESS

is crucial for the absorption efficiency of solar energy. Additionally, the proposed absorber presents bending resistance and its absorption performance remains almost unchanged. The wide-angle and broadband nature of the solar absorber fabricated using the highly efficient and large-area fabrication strategy presents considerable application potential for flexible solar collection devices.

Funding. National Natural Science Foundation of China (11874435, 11904421, 12074443, 62035016); Natural Science Foundation of Guangdong Province (2018B030308005).

Disclosures. The authors declare no conflicts of interest.

Data availability. Data is available from the authors upon reasonable request.

References

1. C. K. N. Peh, M. Gao, and G. W. Ho, "Harvesting broadband absorption of the solar spectrum for enhanced photocatalytic H2 generation," J. Mater. Chem. A **3**(38), 19360–19367 (2015).
2. A. Kumar, K. L. Reddy, S. Kumar, A. Kumar, V. Sharma, and V. Krishnan, "Rational Design and Development of Lanthanide-Doped NaYF4@CdS-Au-RGO as Quaternary Plasmonic Photocatalysts for Harnessing Visible-Near-Infrared Broadband Spectrum," ACS Appl. Mater. Interfaces **10**(18), 15565–15581 (2018).
3. N. Zhang, M. Y. Qi, L. Yuan, X. Fu, Z. R. Tang, J. Gong, and Y. J. Xu, "Broadband Light Harvesting and Unidirectional Electron Flow for Efficient Electron Accumulation for Hydrogen Generation," Angew. Chem. Int. Ed. **58**(29), 10003–10007 (2019).
4. W. Li and J. Valentine, "Metamaterial perfect absorber based hot electron photodetection," Nano Lett. **14**(6), 3510–3514 (2014).
5. Y. Zhai, G. Chen, J. Ji, X. Ma, Z. Wu, Y. Li, and Q. Wang, "Large-scale, broadband absorber based on three-dimensional aluminum nanospike arrays substrate for surface plasmon induced hot electrons photodetection," Nanotechnology **30**(37), 375201 (2019).
6. L. Zhou, C. Zhang, L. Li, T. Liu, K. Li, S. Wu, and X. Li, "Nanobowls-assisted broadband absorber for unbiased Si-based infrared photodetection," Opt. Express **29**(10), 15505–15516 (2021).
7. L. Zhou, Y. Tan, J. Wang, W. Xu, Y. Yuan, W. Cai, S. Zhu, and J. Zhu, "3D self-assembly of aluminium nanoparticles for plasmon-enhanced solar desalination," Nat. Photonics **10**(6), 393–398 (2016).
8. K. Chi, L. Yang, Z. Liu, P. Q. Gao, J. Ye, and S. He, "Large-scale nanostructured low-temperature solar selective absorber," Opt. Lett. **42**(10), 1891–1894 (2017).
9. Y. Liu, J. Qiu, J. Zhao, and L. Liu, "General design method of ultra-broadband perfect absorbers based on magnetic polaritons," Opt. Express **25**(20), A980–A989 (2017).
10. Z. Zhang, Y. Mo, H. Wang, Y. Zhao, and S. Jiang, "High-performance and cost-effective absorber for visible and near-infrared spectrum based on a spherical multilayered dielectric-metal structure," Opt. Lett. **58**(16), 4467–4473 (2019).
11. G. Hou, Z. Wang, Z. Lu, H. Song, J. Xu, and K. Chen, "Enhanced Broadband Plasmonic Absorbers with Tunable Light Management on Flexible Tapered Metasurface," ACS Appl. Mater. Interfaces **12**(50), 56178–56185 (2020).
12. G. Hou, Z. Wang, J. Xu, and K. Chen, "Tungsten-Coated Silicon Nanopillars as Ultra-Broadband and Thermally Robust Solar Harvesting Materials," ACS Appl. Nano Mater. **3**(3), 2430–2437 (2020).
13. G. Liu, X. Liu, J. Chen, Y. Li, L. Shi, G. Fu, and Z. Liu, "Near-unity, full-spectrum, nanoscale solar absorbers and near-perfect blackbody emitters," Solar Energy Materials and Solar Cells **190**, 20–29 (2019).
14. Z. Liu, X. Liu, S. Huang, P. Pan, J. Chen, G. Liu, and G. Gu, "Automatically acquired broadband plasmonic-metamaterial black absorber during the metallic film-formation," ACS Appl. Mater. Interfaces **7**(8), 4962–4968 (2015).
15. L. Zhou, Y. Tan, D. Ji, B. Zhu, P. Zhang, J. Xu, Q. Gan, Z. Yu, and J. Zhu, "Self-assembly of highly efficient, broadband plasmonic absorbers for solar steam generation," Sci. Adv. **2**(4), e1501227 (2016).
16. Y. Zhou, M. Luo, S. Shen, H. Zhang, D. Pu, and L. Chen, "Cost-effective near-perfect absorber at visible frequency based on homogenous meta-surface nickel with two-dimension cylinder array," Opt. Express **26**(21), 27482–27491 (2018).
17. B. J. Lee, L. P. Wang, and Z. M. Zhang, "Coherent thermal emission by excitation of magnetic polaritons between periodic strips and a metallic film," Opt. Express **16**(15), 11328–11336 (2008).
18. X. Han, K. He, Z. He, and Z. Zhang, "Tungsten-based highly selective solar absorber using simple nanodisk array," Opt. Express **25**(24), A1072–A1078 (2017).
19. Y. Li, Z. Liu, H. Zhang, P. Tang, B. Wu, and G. Liu, "Ultra-broadband perfect absorber utilizing refractory materials in metal-insulator composite multilayer stacks," Opt. Express **27**(8), 11809–11818 (2019).
20. P. Tang, G. Liu, X. Liu, G. Fu, Z. Liu, and J. Wang, "Plasmonic wavy surface for ultrathin semiconductor black absorbers," Opt. Express **28**(19), 27764–27773 (2020).
21. Y. Cui, K. H. Fung, J. Xu, H. Ma, Y. Jin, S. He, and N. X. Fang, "Ultrabroadband light absorption by a sawtooth anisotropic metamaterial slab," Nano Lett. **12**(3), 1443–1447 (2012).
22. F. Ding, Y. Jin, B. Li, H. Cheng, L. Mo, and S. He, "Ultrabroadband strong light absorption based on thin multilayered metamaterials," Laser Photonics Rev. **8**(6), 946–953 (2014).

Optics EXPRESS

23. Y. Lin, Y. Cui, F. Ding, K. H. Fung, T. Ji, D. Li, and Y. Hao, "Tungsten based anisotropic metamaterial as an ultra-broadband absorber," Opt. Mater. Express **7**(2), 606–617 (2017).
24. T. Sondergaard, S. M. Novikov, T. Holmgaard, R. L. Eriksen, J. Beermann, Z. Han, K. Pedersen, and S. I. Bozhevolnyi, "Plasmonic black gold by adiabatic nanofocusing and absorption of light in ultra-sharp convex grooves," Nat Commun **3**(1), 969 (2012).
25. J. Beermann, R. L. Eriksen, T. Holmgaard, K. Pedersen, and S. I. Bozhevolnyi, "Plasmonic black metals via radiation absorption by two-dimensional arrays of ultra-sharp convex grooves," Sci Rep **4**(1), 6904 (2015).
26. H. Hulkkonen, A. Sah, and T. Niemi, "All-Metal Broadband Optical Absorbers Based on Block Copolymer Nanolithography," ACS Appl Mater Interfaces **10**(49), 42941–42947 (2018).
27. F. Ding, J. Dai, Y. Chen, J. Zhu, Y. Jin, and S. I. Bozhevolnyi, "Broadband near-infrared metamaterial absorbers utilizing highly lossy metals," Sci Rep **6**(1), 39445 (2016).
28. W. Wang, Y. Qu, K. Du, S. Bai, J. Tian, M. Pan, H. Ye, M. Qiu, and Q. Li, "Broadband optical absorption based on single-sized metal-dielectric-metal plasmonic nanostructures with high-epsilon '' metals," Appl. Phys. Lett. **110**(10), 101101 (2017).
29. M. Chen and Y. He, "Plasmonic nanostructures for broadband solar absorption based on the intrinsic absorption of metals," Solar Energy Materials and Solar Cells **188**, 156–163 (2018).
30. J. Zhao, Y. Wang, Y. Zhu, W. Zhang, and Y. Yu, "Lithography-free flexible perfect broadband absorber in visible light based on an all-dielectric multilayer structure," Opt. Lett. **45**(19), 5464–5467 (2020).
31. J. Wang, J. Dong, Y. Cheng, Z. Xie, and Y. Chen, "Visible to near-infrared nearly perfect absorption from alternate silica and chromium layers deposited by magnetron sputtering," Opt. Lett. **46**(18), 4582–4584 (2021).
32. F. Ding, L. Mo, J. Zhu, and S. He, "Lithography-free, broadband, omnidirectional, and polarization-insensitive thin optical absorber," Appl. Phys. Lett. **106**(6), 061108 (2015).
33. D. Huo, H. Su, C. Wang, X. Ma, and H. Zhao, "Enhanced absorption based on gap-plasmon resonance and Fabry–Perot resonance in a refractory metasurface," J. Opt. Soc. Am. B **38**(4), 1350–1358 (2021).
34. A. D. Rakic, A. B. Djurisic, J. M. Elazar, and M. L. Majewski, "Optical properties of metallic films for vertical-cavity optoelectronic devices," Appl. Opt. **37**(22), 5271–5283 (1998).
35. L. Gao, F. Lemarchand, and M. Lequime, "Exploitation of multiple incidences spectrometric measurements for thin film reverse engineering," Opt. Express **20**(14), 15734–15751 (2012).
36. M. J. Tommalieh and A. M. Zihlif, "Optical properties of polyimide/silica nanocomposite," Phys. B **405**(23), 4750–4754 (2010).
37. Z. M. Zhang, G. Lefever-Button, and F. R. Powell, "Infrared Refractive Index and Extinction Coefficient of Polyimide Films," International Journal of Thermophysics **19**(3), 905–916 (1998).